A Case for an Atmosphere on Super-Earth 55 Cancri e

Isabel Angelo[1,2] and Renyu Hu[1,3]

[1] Jet Propulsion Laboratory, California Institute of Technology, 4800 Oak Grove Drive, Pasadena, CA 91109, USA; renyu.hu@jpl.nasa.gov
[2] Department of Astronomy, University of California, Campbell Hall, #501, Berkeley CA, 94720, USA
[3] Division of Geological and Planetary Sciences, California Institute of Technology, Pasadena, CA 91125, USA

Abstract

One of the primary questions when characterizing Earth-sized and super-Earth-sized exoplanets is whether they have a substantial atmosphere like Earth and Venus or a bare-rock surface like Mercury. Phase curves of the planets in thermal emission provide clues to this question, because a substantial atmosphere would transport heat more efficiently than a bare-rock surface. Analyzing phase-curve photometric data around secondary eclipses has previously been used to study energy transport in the atmospheres of hot Jupiters. Here we use phase curve, *Spitzer* time-series photometry to study the thermal emission properties of the super-Earth exoplanet 55 Cancri e. We utilize a semianalytical framework to fit a physical model to the infrared photometric data at 4.5 μm. The model uses parameters of planetary properties including Bond albedo, heat redistribution efficiency (i.e., ratio between radiative timescale and advective timescale of the atmosphere), and the atmospheric greenhouse factor. The phase curve of 55 Cancri e is dominated by thermal emission with an eastward-shifted hotspot. We determine the heat redistribution efficiency to be $1.47^{+0.30}_{-0.25}$, which implies that the advective timescale is on the same order as the radiative timescale. This requirement cannot be met by the bare-rock planet scenario because heat transport by currents of molten lava would be too slow. The phase curve thus favors the scenario with a substantial atmosphere. Our constraints on the heat redistribution efficiency translate to an atmospheric pressure of ~1.4 bar. The *Spitzer* 4.5 μm band is thus a window into the deep atmosphere of the planet 55 Cancri e.

Key words: occultations – planets and satellites: atmospheres – planets and satellites: individual (55 Cnc e) – planets and satellites: terrestrial planets – techniques: photometric

1. Introduction

Recent successes in exoplanet science can be attributed in part to the development of high precision photometry. Thousands of known exoplanets were first detected using photometric data from space-based missions like *Kepler*, K2, and CoRot, and this number will continue to grow with the next generation of exoplanet detection missions like TESS (Ricker et al. 2016) and PLATO (Rauer et al. 2016). Photometric data are also useful for analysis beyond planet detection. This is because light curves out of transit contain light from reflected stellar radiation and planetary thermal emission. Photometric measurements with *Spitzer* (e.g., Knutson et al. 2007), *Kepler* (e.g., Demory et al. 2013), and *Hubble* (e.g., Stevenson et al. 2014) have provided insight into the properties of exoplanets' atmospheres.

Several previous studies have monitored transiting hot Jupiters during and between transit and occultation (or secondary transit), and used phase curves taken in the visible or infrared wavelengths to determine a variety of planet properties (e.g., Knutson et al. 2007, 2012; Cowan et al. 2012; Demory et al. 2013; Esteves et al. 2013, 2015; Stevenson et al. 2014; Shporer & Hu 2015; Armstrong et al. 2016; Wong et al. 2016; Lewis et al. 2017). These phase curves have provided constraints on the temperature of the planet's atmosphere and the longitudinal location of hotspots. In the cases where a reflected stellar radiation component is detected, the phase curves also constrain the location of clouds. These constraints allow us to further study physical properties of the atmosphere such as circulation patterns, temperature profile, and possible molecular composition.

When it comes to Earth-sized and super-Earth-sized exoplanets that may be predominantly rocky, radiation from the planets may come from either the atmosphere or the surface. If the planet has a substantial atmosphere, the phase-curve signal would be controlled by temperature and cloud distributions in the atmosphere (e.g., Hu et al. 2015; Webber et al. 2015; Parmentier et al. 2016); whereas, if the planet has a bare-rock surface, the phase curve would be controlled by the temperature of the surface and patchy surface features, such as lava lakes that affect the reflectivity (e.g., Kite et al. 2016).

The first phase curve of a super-Earth exoplanet has been detected recently in the infrared (Demory et al. 2016a). The planet 55 Cancri e has a measured mass of $8.08 \pm 0.31\ M_{\oplus}$ and a radius of $1.91 \pm 0.08\ R_{\oplus}$. Interior composition models have found that the measured mass and radius are consistent with a planetary scenario with a massive, high-mean-molecular-weight atmosphere (Demory et al. 2011; Winn et al. 2011), or a volatile-poor planetary scenario with a carbon-rich interior and no atmosphere (Madhusudhan et al. 2012). It is also known that the planet does not have an extended, H-rich exosphere (Ehrenreich et al. 2012), which excludes the possibility of an H-rich atmosphere, but does not exclude the high-mean-molecular-weight atmosphere scenario. There have been searches for molecular features of 55 Cancri e, using transit spectroscopy in the infrared (Tsiaras et al. 2016) and high-resolution optical spectroscopy (Esteves et al. 2017), but results are nonconclusive. The phase curve of 55 Cancri e, taken in the *Spitzer* Infrared Array Camera (IRAC) 2 band of 4–5 μm, features a peak of the planet's radiation occurring prior to the occultation, and a large day–night temperature contrast. Demory et al. (2016a) hypothesized that the phase curve could be explained by either a planet with an optically thick, high-mean-molecular-weight atmosphere, or a planet devoid of atmosphere with low-viscosity magma flows.

In this paper, we utilize a physical model developed by Hu et al. (2015) to analyze the phase curve for 55 Cancri e. The purpose of our study is to augment the results of Demory et al. (2016a) by using the same data set to fit for a more physically motivated model and derive improved constraints on the planet's heat redistribution. Our reanalysis of the phase curve suggests that the planet has a substantial atmosphere and the *Spitzer* IRAC 2 band is a window into the pressure level as deep as 1–2 bars. We first outline our data preparation and model fitting in Section 2. The results of our analysis are presented in Section 3. In Section 4, we interpret these results and discuss their implications on the planetary scenarios. Finally, we summarize our findings and discuss prospects for future research in Section 5.

2. Analysis

2.1. Observations

For our analysis, we use the same photometric data as Demory et al. (2016a), taken by the *Spitzer Space Telescope* Infrared Camera (IRAC 2) at 4.5 μm. Observations during the primary transit and occultation of 55 Cancri e were taken between 2013 June 15 and July 15. A total of 4,981,760 frames were obtained with an integration time of 0.02 s. The frames were taken during eight observing sessions of 9 hr each (half of the planet's orbital period), yielding a total observation time of 75 hr.

2.2. Data Reduction and Preparation

Once the observations were obtained from *Spitzer*, they needed to be converted into a photometric time series from which we can perform phase-curve analysis and modeling. The raw photometric time series was computed from the individual frames by Demory et al. (2016a) using methods outlined in Demory et al. (2011). These raw data were subject to noise from the IRAC detector itself as well as correlated noise from *Spitzer* as it moves during observation. This noise was removed from our data set by Demory et al. (2016a) to produce a final time series of 30 s bins with an average error that we calculate to be ~360 parts per million.

After the raw frames were converted into photometric time-series data, we then binned the data to 200 bins for improved visual inspection. The flux value $F_p/F_\star$ relative to the in-occultation stellar flux for each bin was computed by averaging the 30 s flux values for each sample. Uncertainties in each bin were computed by dividing the standard deviation of the sample by the square root of the total sample size per bin, yielding an average bin error of ~56 parts per million. We then phase-folded our time-series data and removed data taken during primary transits that are not accounted for in the phase-curve model we implemented. While not fitting the primary transits, we use the constraints from the primary transits on planetary radius, semimajor axis, and impact parameter in the subsequent phase-curve modeling (see Section 2.3). Our photometric time series is shown in Figure 1.

Several effects beyond those of planetary atmospheric processes can determine the properties of an occultation phase curve. For example, stellar variability brought about by magnetic field interactions with the planet can cause star spots with a period similar to the planet's orbital period (Shkolnik et al. 2008). Additionally, gravitational interactions between a star and its planetary companion can produce effects such as

relativistic beaming and tidal ellipsoidal distortion modulations that can alter the phase curve (e.g., Shporer & Hu 2015; Shporer 2017). These processes do not produce significant effects on the infrared light curve for 55 Cancri e (e.g., beaming modulation ~1 ppm, ellipsoidal modulation ~0.6 ppm; Demory et al. 2016a). We therefore make no corrections to our sample to account for these effects. Furthermore, the orbit of 55 Cancri e can be approximated as circular ($e \approx 0.040 \pm 0.027$, see Baluev 2015), allowing us to use a model fitting method in line with that of Hu et al. (2015).

One must be cautious when binning time-series photometric data for phase-curve analysis to prevent loss or distortion of information (e.g., Kipping 2010). We have additionally computed model fits for the same data with a much smaller bin size (the native 30 s bins), and with a larger bin size similar to the phase curve in Demory et al. (2016a; a total of ≈70 bins of in- and out-of-transit data). The constraints on the jump parameters are identical to the 200-bin data set to within uncertainty limits, confirming that our model fit does not depend on the binning of the data. We therefore proceed with our analysis using only results from the ≈200-bin data set described above.

2.3. Phase-curve Modeling

To perform our model fit to the photometric data, we use a semianalytical method outlined in Hu et al. (2015). The general model performs a fit to the occultation light curve of a planet and also computes three independent light curves representing flux contributions from symmetric reflection, asymmetric reflection (e.g., due to patchy clouds), and thermal emission. It also uses an existing model of secondary transit (Mandel & Agol 2002) from which it can derive the phase-curve occultation depth, phase amplitude, and phase offset.

As shown in Hu et al. (2015), the scaled total reflective component (i.e., symmetric + asymmetric) of the transiting planet $\frac{F_R}{F_\star}$ is computed as follows

$$\frac{F_R}{F_\star} = A_G \left(\frac{R_p}{a}\right)^2, \qquad (1)$$

where A_G is the uniform geometric albedo of the planet, R_p is the planet radius, and a is the semimajor axis of the planet's orbit. This means that the contribution of the reflective components to the planet's phase curve is largely governed by the magnitude of $\left(\frac{R_p}{a}\right)^2$. For 55 Cancri e, using values for R_p and a found in Demory et al. (2016a), we find that this value is 2.77×10^{-5}, or ≈28 parts per million (p.p.m.). This value, even with a geometric albedo of 1, would thus contribute no more than 28 p.p.m. to our final model fit, which takes on much larger flux fluctuations ~200 p.p.m. The data, with a dispersion of 56 ppm, are too noisy to detect any reflected light component. It is also not possible to distinguish between uniform and patchy reflective clouds or surfaces, because the asymmetric reflection component would make a contribution much smaller than 28 ppm to the light curve. We therefore assume for the purposes of this paper a purely symmetric reflection component and take the asymmetric component of the reflection contribution to be zero at all phase values.

The general model fit computes the posterior distributions of three to five parameters from the phase curve. The first is the
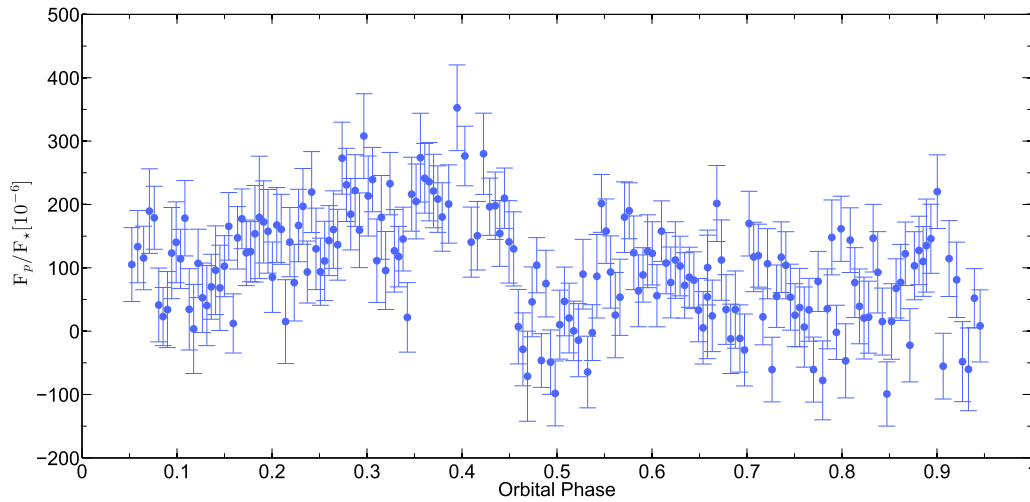
Figure 1. Occultation photometric time-series data for 55 Cancri e. Data points represent scaled planet flux $F_p/F_\star$ in parts per million (ppm) and are plotted vs. orbital phase, with a phase of 0.5 corresponding to secondary transit. Data are binned per 20 minutes, and each flux value represents the bin sample mean. The uncertainty for each point was calculated by taking the true standard deviation of the bin sample mean $\frac{\sigma}{\sqrt{N}}$.

Bond albedo (A_B), which is a measurement of the fraction of incident light on the planet that is scattered back into space. The second, referred to as the heat redistribution efficiency (ϵ), is defined as

$$\epsilon = \frac{\tau_{\rm rad}}{\tau_{\rm adv}}, \qquad (2)$$

where $\tau_{\rm rad}$ is the radiative timescale and $\tau_{\rm adv}$ is the advective timescale (Cowan & Agol 2011; Hu et al. 2015). This parameter describes how well heat is transported from the planet's dayside to nightside. When $|\epsilon| \gg 1$ heat transport is more efficient than radiative cooling and the longitudinal variation of temperature will be small, corresponding to giant planets in the solar system; when $|\epsilon| \ll 1$ transport is minimal and the planet will be in local thermal equilibrium, leading to large day–night contrast (Cowan & Agol 2011). The sign of ϵ is the same as the sign of $\tau_{\rm adv}$, which indicates the direction of transport and the thermal phase shift: when $\epsilon > 0$, the transport is eastward and the peak of the thermal emission appears prior to the occultation; when $\epsilon < 0$, the transport is westward and the peak of the thermal emission appears after the occultation. The magnitude of the radiative timescale depends on the heat capacity and the temperature, and the magnitude of the advective timescale is determined by the speed of fluid movement (atmosphere or molten lava), which is discussed further in Section 4.

The third parameter is the greenhouse factor (f), a measurement of the extent to which infrared radiation is absorbed by greenhouse gases in the atmosphere. It is defined as the ratio between the brightness temperature of the photosphere and the equilibrium temperature. The last two parameters are the cloud condensation temperature (T_c), under which the atmosphere precipitates and forms patchy clouds, and the reflectivity boosting factor (κ), which describes the proportional increase in the reflectivity of the clouds in the atmosphere. The first three parameters (A_B, ϵ, f) are computed for each model, while the last two (T_c and κ) are only relevant in the scenario in which the planet has a patchy cloud covering (see Hu et al. 2015 for more details). Because we are assuming the surface of the planet to be symmetrically reflective (i.e.,

without a patchy cloud or lava lake), T_c and κ are not used by the phase-curve model. We are thus performing a model fit that depends on three free parameters: Bond albedo, heat redistribution efficiency, and greenhouse factor.

The methods developed and outlined in Hu et al. (2015) use a Markov Chain Monte Carlo (MCMC) to compute both the fitted parameters and their posterior distributions. We first input the allowed ranges within which the MCMC can sample for each parameter. The Bond albedo is defined as a fraction that naturally ranges in [0, 1]. The heat redistribution ϵ is allowed to range between -100 and 100, where the sign is determined by the direction of the photosphere rotation with respect to the planet's orbit. For the atmospheric greenhouse factor f, we allowed a range of [1, 2] with 1 corresponding to no greenhouse effect and 2 corresponding to a thermal photosphere temperature two times greater than the planet's equilibrium temperature. Allowing $f > 2$ is not necessary because the temperature of the planet does not have to double even for A_B approaching 1 (see Section 3.2). These input ranges are wide enough and do not cause distortion in the parameters' posterior distributions; we confirm this by inspecting the output of the Markov chains, which shows that the posterior distributions are narrower than the prior ranges (Figures 3 and 4).

In addition to the allowed ranges for the fitted parameters, we input values for system parameters that the algorithm uses to compute the model phase curves. We use an empirical and absolutely calibrated infrared spectrum of 55 Cancri (Crossfield 2012) to compute the stellar flux in the IRAC 4.5 μm bandpass, and also use the scaled semimajor axis ($a/R_\star$), the ratio between the planet's radius and the star's radius ($R_p/R_\star$), and the impact parameter (b) constrained by primary transit observations (Demory et al. 2011, 2016a; von Braun et al. 2011). We use the value of $R_p/R_\star$ measured from the same observation as the phase curve (Demory et al. 2016b), which is 365 ± 25 ppm, corresponding to $R_p/R_\star = 0.0191 \pm 0.0007$, in our analysis. The stellar luminosities and orbital parameters are known to high precisions, and they make negligible contributions to the uncertainties of our fitted parameters. The planetary radius is more uncertain and we thus propagate its uncertainty to the fitted parameters in Section 3.2.

Table 1
Fitted and Derived Parameters for 55 Cancri e[a]

Parameter	Value
Derived Parameters	
Phase amplitude (ppm)	127^{+12}_{-14}
Eclipse depth (ppm)	181^{+15}_{-19}
Phase offset (degree)[b]	-34^{+4}_{-5}
Fitted Parameters	
Bond albedo A_B	$0.43^{+0.32}_{-0.29}$
Heat redistribution ϵ[c]	$1.47^{+0.30}_{-0.25}$
Greenhouse factor f	$1.31^{+0.28}_{-0.13}$
Calculated Surface Temperatures	
Maximum hemisphere-averaged temperature (K)	2709^{+129}_{-159}
Minimum hemisphere-averaged temperature (K)	1613^{+118}_{-131}
Average dayside temperature (K)	2573^{+120}_{-153}

Notes.
[a] The best-fit model has χ^2/dof of 1.14.
[b] Defined to be positive for post-occultation maximum.
[c] Defined to be positive for eastward-traveling winds in a synchronously rotating reference frame.

Next we computed two separate Markov chains, each with 100,000 steps representing different combinations of the fitted parameters. The first half of each chain, which we refer to as the "burn-in" period, was discarded from our final results. We then confirmed the robustness of our final results by verifying their convergence (i.e., assuring $R < 1.01$ for all parameters, as described in Gelman & Rubin 1992).

3. Results

3.1. Light -curve Parameters

The fitted and derived system parameters for 55 Cancri e are listed in Table 1. The values for these parameters were computed by taking the median of the posterior distribution generated by the MCMC analysis (see Section 2.3). The final model fit and residuals computed from these parameters are plotted against our occultation data in Figure 2. From the model fit, we can see that the phase curve of 55 Cancri e is dominated by thermal emission with no significant contribution from the reflected light. We can also see that the fit to the light curve is not symmetric about the secondary transit. Instead, there is a phase curve maximum that occurs pre-occultation at an offset of $\approx -34°$.

The phase-curve model from Hu et al. (2015) generates the amplitude, occultation depth, and offset based on the fit to the observed data (see Table 1). Errors for all values in Table 1 were computed using the values 1 standard deviation above and below the mean, corresponding to z scores of ± 1 for a standard normal distribution. Here we measure our phase-curve amplitude to be 127^{+12}_{-14} p.p.m. This value is $\approx 2\sigma$ smaller but better constrained than the amplitude found in Demory et al. (2016a). For our eclipse depth, we derive a value of 181^{+15}_{-19} p.p. m., which is 1σ greater than the value derived in Demory et al. (2016a). Upon inspection of the model phase curves in Demory et al. (2016a), the best-fit models look similar at the peak ($\frac{F_p}{F_\star}$ around ~ 200 p.p.m.), but our best-fit model indicates a minimum out-of-transit value of ~ 70 p.p.m., as opposed to ~ 50 p.p.m. of Demory et al. (2016a). The difference is mostly due to the different models used in the phase-curve analysis.

Demory et al. (2016a) used a single-longitude-band model and a three-longitude-band model to fit the phase curve, and their models have sharp temperature discontinuities between the bands. Our model does not allow for these discontinuities and instead calculates a smooth longitudinal distribution of temperature by solving an energy transport equation (see Hu et al. 2015). Our physically motivated model provides a good fit to the phase curve, and indicates a smaller phase amplitude and a higher nightside temperature than Demory et al. (2016a). This analysis thus highlights the need to use a physically motivated model in the phase-curve analysis compared to the longitudinal band models.

Our third derived parameter is the phase-curve offset, defined to be positive when the phase-curve maximum occurs post-occultation. We find a pre-occultation phase curve offset of -34^{+4}_{-5} degrees, which agrees with the offset from Demory et al. (2016a) to within error estimates. Because the phase curve is dominated by contributions from thermal emission (Figure 2), the offset is likely due to a hotspot located east of the substellar point (see Section 4 for more details).

The posterior probability distributions for our fitted model parameters are shown in the top three panels of Figure 3. As we can see, the three derived parameters discussed above are tightly constrained in the scenario to which we fit our model curve. In other words, the phase-curve amplitude, offset, and occultation depth are well constrained to the values listed in Table 1.

We also used our derived phase-curve parameters to compute a series of surface temperatures for the planet (Table 1). We used the eclipse depth to compute an average dayside temperature of 2573^{+120}_{-153} K. From the phase-curve amplitude we calculate a minimum and maximum hemisphere-averaged temperature of 2709^{+129}_{-159} K and 1613^{+118}_{-131} K respectively. All of these values agree with those found in Demory et al. (2016a) to within 1σ, but we compute a higher nightside temperature and a smaller day–night temperature contrast of ~ 950 K that is more in line with the presence of a convective envelope. The fact that our maximum hemisphere-average temperature is greater than the average dayside temperature is consistent with our phase-curve offset of -34^{+4}_{-5} and is likely due to an eastward-shifted hotspot. These implications are discussed further in Section 4.

3.2. Model Parameters

In addition to the derived parameters discussed in Section 3.1, the model phase curve contains enough information to compute a set of fitted planetary parameters (see Section 2.3). In the case of a homogeneous reflective layer, the model outputs estimates for the planet's Bond albedo A_B, heat redistribution efficiency ϵ, and greenhouse factor f. The fitted values for these parameters can be found in Table 1.

The posterior probability distributions of the fitted planetary parameters for 55 Cancri e can be found in the three bottom panels of Figure 3. As we can see, the value for the heat redistribution efficiency (middle panel) is well constrained between 1 and 3 at an estimated value of $\epsilon = 1.47^{+0.30}_{-0.25}$. A positive value for ϵ at almost 5σ above zero indicates that the advective frequency of the planet's envelope is nonzero and consequently that material at photospheric pressures above the planet's surface travel eastward in a synchronously rotating frame. The magnitude of ϵ is inconsistent with a lava ocean and
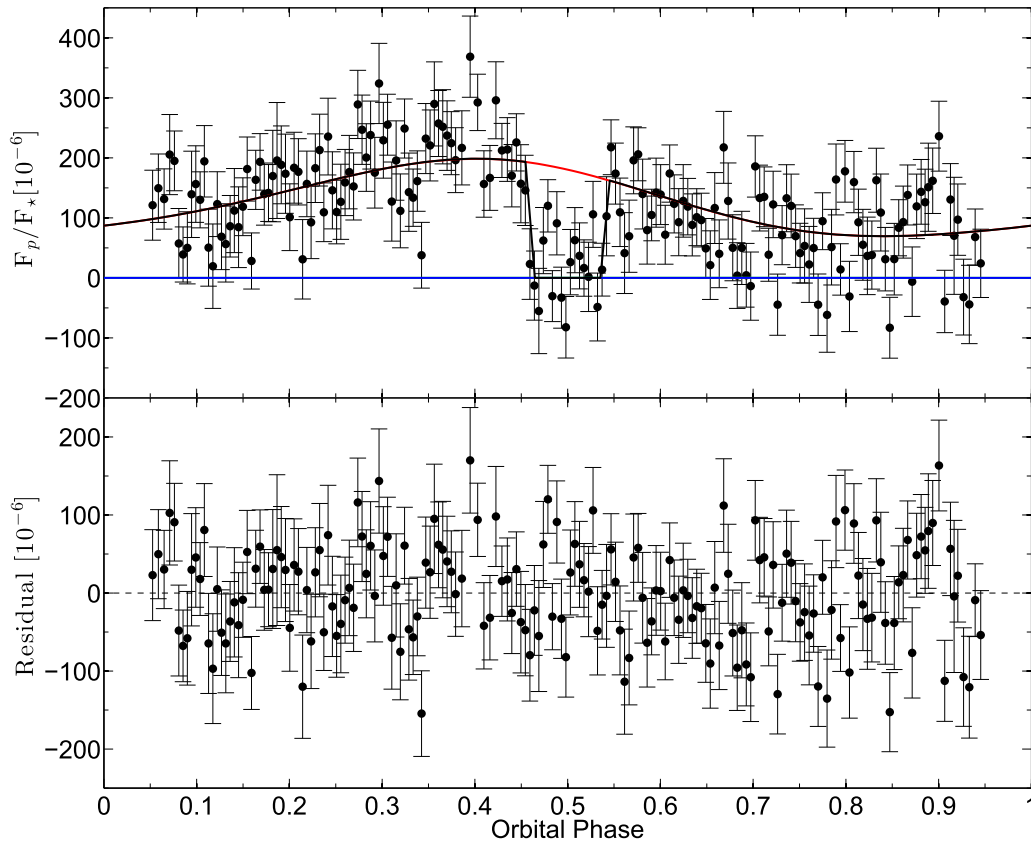
Figure 2. Top panel shows the model fit to our phase curve plotted against photometric data from Figure 1. The black curve represents the best-fit model phase curve, and the rest show flux contributions from thermal emission (red) and reflection (blue). The model fit is governed primarily by the planet's thermal emission and has an asymmetry due to an eastward-shifted hotspot. In the bottom panel, the residuals of the model fit are plotted for each of the photometric data points.

thus suggestive of a thick atmosphere. This scenario is discussed in more detail in Section 4.

As we can tell by inspection of Figure 3, the Bond albedo and greenhouse factor do not have the same narrow distribution as ϵ, and they are not constrained independently. The planet's Bond albedo A_B can take any value smaller than 0.9. Similarly, the atmospheric greenhouse factor f is typically closer to 1.2 but also takes essentially all of the allowed values between 1 and 2. The two parameters are correlated, as shown in Figure 4. This is due to the proportionality from Hu et al. (2015), viz.

$$T \propto f(1 - A_B)^{1/4}, \qquad (3)$$

which our model uses to compute the temperature distribution on the planet's surface. As we can see from Equation (2), raising f requires an additional increase in A_B for a given temperature and vice versa. This is in line with what we see in Figure 4, where a lower $A_B \approx 0.1$ corresponds to lower $f \leqslant 1.3$ and f slowly leveling off at 2 as A_B approaches 1. Additionally, the fact that $f > 2$ corresponds to a forbidden Bond albedo greater than 1 further motivates our allowed ranges for f in our model fit of [1, 2].

The uncertainty in the planetary radius (8% in terms of $(R_p/R_\star)^2$) has an impact on the derived temperatures, and thus the greenhouse factor f. We propagate this uncertainty by calculating the brightness temperatures corresponding to the 1σ upper and the lower bounds of the planetary radius, and find that this would increase the uncertainty in the dayside and nightside temperatures by 50 K and 20 K respectively. This in turn causes the uncertainty in the greenhouse factor to increase

by 0.04, in addition to 0.28 as tabulated in Table 1. The uncertainty in the planetary radius thus has no impact on the general results.

4. Discussion

The model fit to our *Spitzer* light curve for 55 Cancri e is composed primarily of planetary thermal emission with a negligible contribution from reflected light of the host star. The fitted light curve also shows a pre-occultation phase shift of $-34^{+4}_{-5}°$. Because the planetary light is dominated by thermal emission, we interpret this shift to be due to an eastward-shifted hotspot on the planet surface. This, in conjunction with our positive fitted value for heat redistribution efficiency $\epsilon = 1.47^{+0.30}_{-0.25}$ and our divergent values for dayside and maximum temperatures, suggests eastward heat transport via advection in the planet's outer envelope.

Our fitted value for ϵ indicates that the advective timescale is on the same order as the radiative timescale, and implies a thick atmosphere around 55 Cancri e. There are two possible planetary scenarios that determine the value of τ_{adv}. The first is the scenario in which heat is primarily transported by currents in magma lakes. Kite et al. (2016) has estimated the speed of the magma currents driven by the day–night temperature contrast on hot, rocky exoplanets. Neglecting viscosity and inertia, the speed is controlled by the balance between the pressure gradient and the rotational force (i.e., geostrophic balance). The speed is found to be low ($\sim 0.02\,\mathrm{m\,s^{-1}}$), requiring ~ 10 years for heat to be transport from the dayside to the nightside. The slow transport is due to the very small
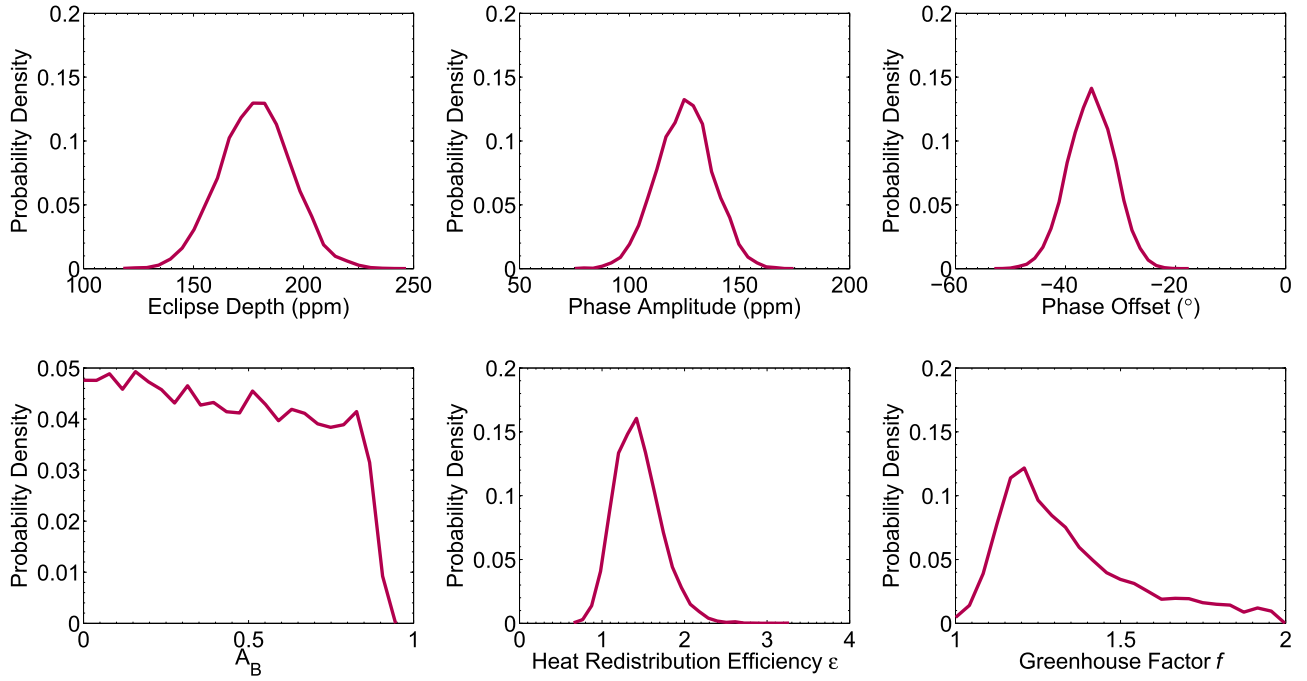
Figure 3. Posterior probability distributions for the derived (top) and fitted (bottom) parameters from our MCMC phase-curve analysis are plotted for 55 Cancri e. Of the derived parameters, the phase offset of -34^{+4}_{-5} (top right) is best constrained to within 13% while the eclipse depth and phase amplitude (top left and middle) are constrained to within $\approx 10\%$ their estimated values. For the fitted parameters, the heat redistribution efficiency $\epsilon = 1.47^{+0.30}_{-0.25}$ has a relatively normal spread ranging in $\approx 20\%$ while the bond albedo and greenhouse factor have less regular distributions.
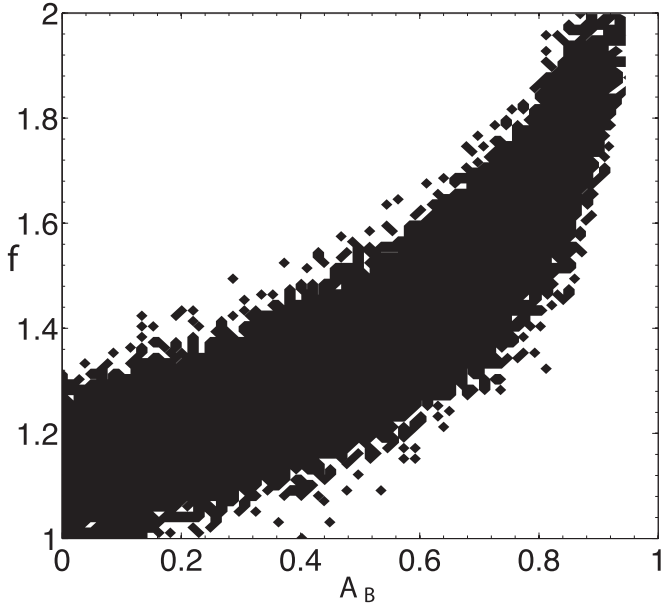

Figure 4. Correlation between Bond albedo A_B and greenhouse factor f shows that larger greenhouse effect corresponds to a larger overall planet reflectivity. We see that smaller $A_B \approx 0.5$ corresponds to little to no greenhouse affect at $f \approx 1$. Additionally, f quickly approaches 2 as A_B gets closer to 1, a nonphysical case for planet atmospheres.

expansivity of the magma, and then the very small density contrast, compared with an atmosphere. As such, this estimate is independent from the composition of the magma. With our ϵ value in this case, the radiative timescale would need to be on the order of tens of years, far too long given a dayside temperature >2000 K (Table 1). The phase curve thus disfavors the scenario in which heat on 55 Cancri e is transported primarily via lava lakes.

The second possible scenario is that heat is transported convection in a thick atmospheric envelope. In this case, the advective timescale $\tau_{\rm adv} = R_p / v_w$. Using a planet radius of $R_p = 1.91 \, R_{\oplus}$ and wind speed of $1000 \, {\rm m \, s}^{-1}$ typically obtained in GCMs for high-mean-molecular-weight atmospheres (e.g., Zhang & Showman 2017), we compute an advective timescale of $\tau_{\rm adv} \sim 3$ hr, suggesting that the radiative timescale would need to be on the order of hours, a much more plausible scenario than that of heat transport by lava lakes.

The radiative timescale of an atmosphere is related to the photospheric-level pressure P as

$$\tau_{\rm rad} = \epsilon \times \tau_{\rm adv} = \frac{c_p P}{g \sigma T_0^3}, \qquad (4)$$

where c_p is the specific heat capacity, g is the surface gravity, σ is the Stefan–Boltzmann constant, and T_0 is the temperature of radiation for which we approximate the average dayside temperature (Table 1). We deduce from Equation (4) that the photosphere would need to be at a pressure of $P \approx 1.4$ bar based on the measured value of ϵ.

Is this photospheric pressure reasonable for the *Spitzer* observation in 4–5 μm? Table 2 lists several hypothetical atmospheric scenarios and their opacities based on simple C-H-O-N-S molecules. The optical depth at 1.4 bar needs to be on the order of, or smaller than, unity in order to be consistent with the photospheric pressure. We see that H_2O- or CO_2-dominated atmospheres are not possible because of their strong absorption in this wavelength range. However, a CO- or N_2-dominated atmosphere is possible. If the atmosphere is made of N_2, it should also contain ~0.2% of H_2O or 2% of CO_2 to cause the photosphere to be at 1.4 bar. Such abundances of H_2O or CO_2 seem reasonable for an N_2-dominated atmosphere. We also note that an evaporation atmosphere in vapor equilibrium with the magma (made of Na, O_2, SiO, Mg, and Fe) would have a

Table 2
Opacities of the Hypothetical Atmospheric Scenarios of 55 Cancri e

Type of Atmosphere	Source of Opacity	τ at 1.4 bar
H_2O-dominated	H_2O	450
N_2-dominated	N_2-N_2 CIA	0.06
CO_2-dominated	CO_2	38
CO-dominated	CO	1.2
O_2-dominated	O_3	0.8

Note. The optical depth is the column-integrated opacity at 1.4 bar, averaged over the *Spitzer* IRAC 4.5 μm bandpass. The opacities are adopted from the HITRAN 2012 and HITEMP 2010 databases (Rothman et al. 2010, 2013). The temperature is assumed to be 2000 K for simplicity. CIA stands for collision-induced absorption. O_3 is assumed to be photochemically produced and is 10^{-3} of the abundance of O_2 (e.g., Hu et al. 2012).

total surface pressure of $10^{-3} \sim 10^{-2}$ bar depending on the composition of the underlying magma (Schaefer & Fegley 2009). Such a tenuous vapor atmosphere cannot transport heat fast enough (e.g., Kite et al. 2016) and thus cannot explain the phase-curve features.

Therefore, the phase curve implies that, at *Spitzer* wavelengths around 4.5 μm, we are able to see deep into the planet atmosphere. The atmosphere is clear in this band and cannot have dominated abundances of CO_2 or H_2O that have strong absorption at the observed wavelengths (Table 2, also see Hu & Seager 2014). It remains possible that the planet is engulfed by a CO- or N_2-dominated envelope. Our analysis supports the case of an atmosphere around 55 Cancri e.

One might ask whether a CO- or N_2-dominated envelope on the planet 55 Cancri e is stable against intense irradiation that would drive atmospheric escape. Assuming energy-limited escape, Demory et al. (2016a) estimated that a total of 31 kbar worth of atmosphere would have been lost due to stellar irradiation if the planet has a substantial atmosphere. We stress, however, that this 31 kbar corresponds to only 0.5% of the mass of the planet, while it is not uncommon to find volatile content greater than 2% in building blocks of terrestrial planets (e.g., Elkins-Tanton & Seager 2008). The total escape was also likely an overestimate, because the energy-limited escape formula does not apply to the transonic escape regime at high irradiation, as is the case for 55 Cancri e (Johnson et al. 2013). In this regime, the escape flow has high kinetic energy, but the escape rate is low. Therefore, we suggest a CO- or N_2-dominated envelope as a plausible scenario for the planet 55 Cancri e.

5. Conclusion

We present an analysis of the infrared *Spitzer* phase curve for the super-Earth 55 Cancri e. We fit a theoretical light curve to the photometric time series taken at 4.5 μm using physical models developed in Hu et al. (2015). With physically motivated models, our analysis of the phase curve of 55 Cancri e confirms and further constrains the eclipse depth and phase offset reported by Demory et al. (2016a) and estimates a smaller phase amplitude and higher nightside temperature than previously found.

The *Spitzer* phase curve for 55 Cancri e is dominated by thermal emission with a pre-occultation shift due to a hotspot located east of the substellar point. The planet's heat redistribution efficiency constrained by the phase curve $\epsilon = 1.47^{+0.30}_{-0.25}$ requires that 55 Cancri e is shrouded by a thick atmosphere that acts as a primary source of heat transport. This value corresponds to a photospheric pressure of 1.4 bar, consistent with a CO- or N_2-dominated atmosphere, with minor abundances of H_2O or CO_2.

The *Spitzer* light curve used in both our analysis and Demory et al. (2016a) represents the first phase curve of a super-Earth-sized exoplanet, reflecting recent progress in observing technology and methods. Our analysis of 55 Cancri e will be the first of many, and further observations of super-Earths in the coming years will set up a context in which our results can be further interpreted. Additionally, photometric observations of 55 Cancri e in other wavelengths may shed light and place further constraints on the planetary characteristics found in this paper. We therefore are optimistic that further research will illuminate the nature of 55 Cancri e's atmosphere and super-Earths alike.

ORCID iDs

Isabel Angelo https://orcid.org/0000-0002-9751-2664

References

Armstrong, D. J., de Mooij, E., Barstow, J., et al. 2016, NatAs, 1, 0004
Baluev, R. V. 2015, MNRAS, 446, 1493
Cowan, N. B., & Agol, E. 2011, ApJ, 726, 82
Cowan, N. B., Machalek, P., Croll, B., et al. 2012, ApJ, 747, 82
Crossfield, I. J. M. 2012, A&A, 545, A97
Demory, B.-O., de Wit, J., Lewis, N., et al. 2013, ApJL, 776, L25
Demory, B.-O., Gillon, M., de Wit, J., et al. 2016a, Natur, 532, 207
Demory, B.-O., Gillon, M., Deming, D., et al. 2011, A&A, 533, A114
Demory, B.-O., Gillon, M., Madhusudhan, N., & Queloz, D. 2016b, MNRAS, 455, 2018
Ehrenreich, D., Bourrier, V., Bonfils, X., et al. 2012, A&A, 547, A18
Elkins-Tanton, L. T., & Seager, S. 2008, ApJ, 685, 1237
Esteves, L. J., De Mooij, E. J. W., & Jayawardhana, R. 2013, ApJ, 772, 51
Esteves, L. J., De Mooij, E. J. W., & Jayawardhana, R. 2015, ApJ, 804, 150
Esteves, L. J., de Mooij, E. J. W., Jayawardhana, R., Watson, C., & de Kok, R. 2017, AJ, 153, 268
Gelman, A., & Rubin, D. B. 1992, StaSc, 7, 457
Hu, R., Demory, B.-O., Seager, S., Lewis, N., & Showman, A. P. 2015, ApJ, 802, 51
Hu, R., & Seager, S. 2014, ApJ, 784, 63
Hu, R., Seager, S., & Bains, W. 2012, ApJ, 761, 166
Johnson, R. E., Volkov, A. N., & Erwin, J. T. 2013, ApJL, 768, L4
Kipping, D. M. 2010, MNRAS, 408, 1758
Kite, E. S., Fegley, B., Jr., Schaefer, L., & Gaidos, E. 2016, ApJ, 828, 80
Knutson, H. A., Charbonneau, D., Allen, L. E., et al. 2007, Natur, 447, 183
Knutson, H. A., Lewis, N., Fortney, J. J., et al. 2012, ApJ, 754, 22
Lewis, N. K., Parmentier, V., Kataria, T., et al. 2017, AJ, submitted, arXiv:1706.00466
Madhusudhan, N., Lee, K. K. M., & Mousis, O. 2012, ApJL, 759, L40
Mandel, K., & Agol, E. 2002, ApJL, 580, L171
Parmentier, V., Fortney, J. J., Showman, A. P., Morley, C., & Marley, M. S. 2016, ApJ, 828, 22
Rauer, H., Aerts, C., Cabrera, J. & PLATO Team 2016, AN, 337, 961
Ricker, G. R., Vanderspek, R., Winn, J., et al. 2016, Proc. SPIE, 9904, 99042B
Rothman, L., Gordon, I., Barber, R., et al. 2010, JQSRT, 111, 2139
Rothman, L. S., Gordon, I. E., Babikov, Y., et al. 2013, JQSRT, 130, 4
Schaefer, L., & Fegley, B. 2009, ApJL, 703, L113
Shkolnik, E., Bohlender, D. A., Walker, G. A. H., & Collier Cameron, A. 2008, ApJ, 676, 628
Shporer, A. 2017, PASP, 129, 072001
Shporer, A., & Hu, R. 2015, AJ, 150, 112

Stevenson, K. B., Désert, J.-M., Line, M. R., et al. 2014, Sci, 346, 838
Tsiaras, A., Rocchetto, M., Waldmann, I. P., et al. 2016, ApJ, 820, 99
von Braun, K., Boyajian, T. S., ten Brummelaar, T. A., et al. 2011, ApJ, 740, 49

Webber, M. W., Lewis, N. K., Marley, M., et al. 2015, ApJ, 804, 94
Winn, J. N., Matthews, J. M., Dawson, R. I., et al. 2011, ApJL, 737, L18
Wong, I., Knutson, H. A., Kataria, T., et al. 2016, ApJ, 823, 122
Zhang, X., & Showman, A. P. 2017, ApJ, 836, 73